



Journal of Geophysical Research: Solid Earth

Supporting Information for

Rupture Directivity of the 2021 M_W 6.0 Yangbi, Yunnan Earthquake

Wenzheng Gong¹, Lingling Ye^{1,*}, Yuxin Qiu¹, Thorne Lay², and Hiroo Kanamori³

¹Department of Earth and Space Sciences, Southern University of Science and Technology, Shenzhen, Guangdong, 518055, China.

²Department of Earth and Planetary Sciences, University of California Santa Cruz, Santa Cruz, California, 95064, USA.

³Seismological Laboratory, California Institute of Technology, Pasadena, California, 91125, USA.

Contents of this file

Figures S1 to S12

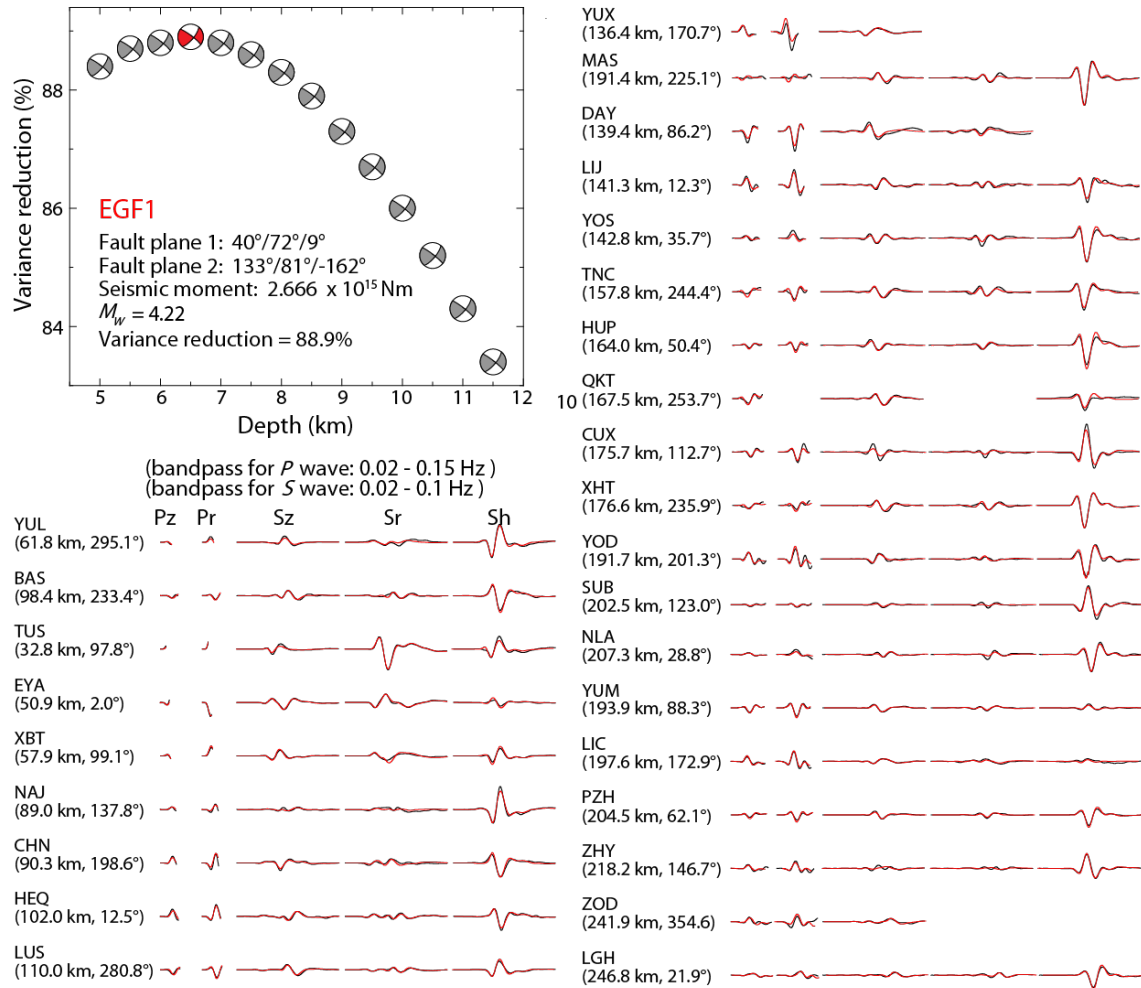


Figure S1. Point-source focal mechanism inversion for the EGF1 earthquake. The focal mechanism was inverted by the CAP method for point sources varying in depth from 5.0 km to 11.5 km. The centroid location is fixed at $(25.65^\circ\text{N}, 99.93^\circ\text{E})$ from the YEA catalog. Waveform fitting for the solution at the optimal depth at 6.5 km are shown. The indicated bandpass filters have been applied to the P and S seismogram segments. The distance (km) and azimuth ($^\circ$) for each station are indicated. Black and red traces show the data and synthetics, respectively.

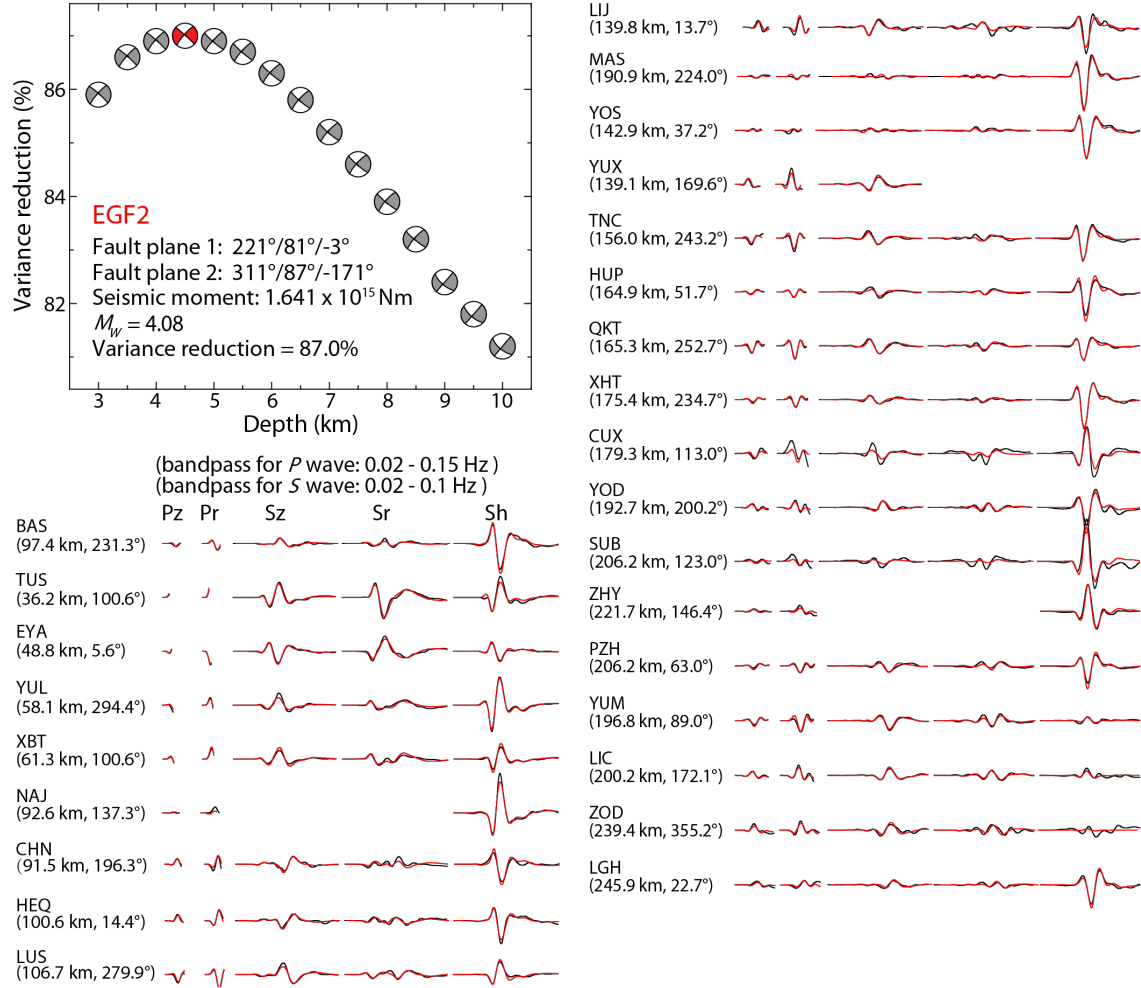


Figure S2. Point-source focal mechanism inversion for the EGF2 earthquake. The focal mechanism was inverted by the CAP method for point sources varying in depth from 3.0 km to 9.5 km. The centroid location is fixed at (25.67°N, 99.90°E) from the YEA catalog. Waveform fitting for the solution at the optimal depth at 4.5 km are shown. The indicated bandpass filters have been applied to the *P* and *S* seismogram segments. The distance (km) and azimuth (°) for each station are indicated. Black and red traces show the data and synthetics, respectively.

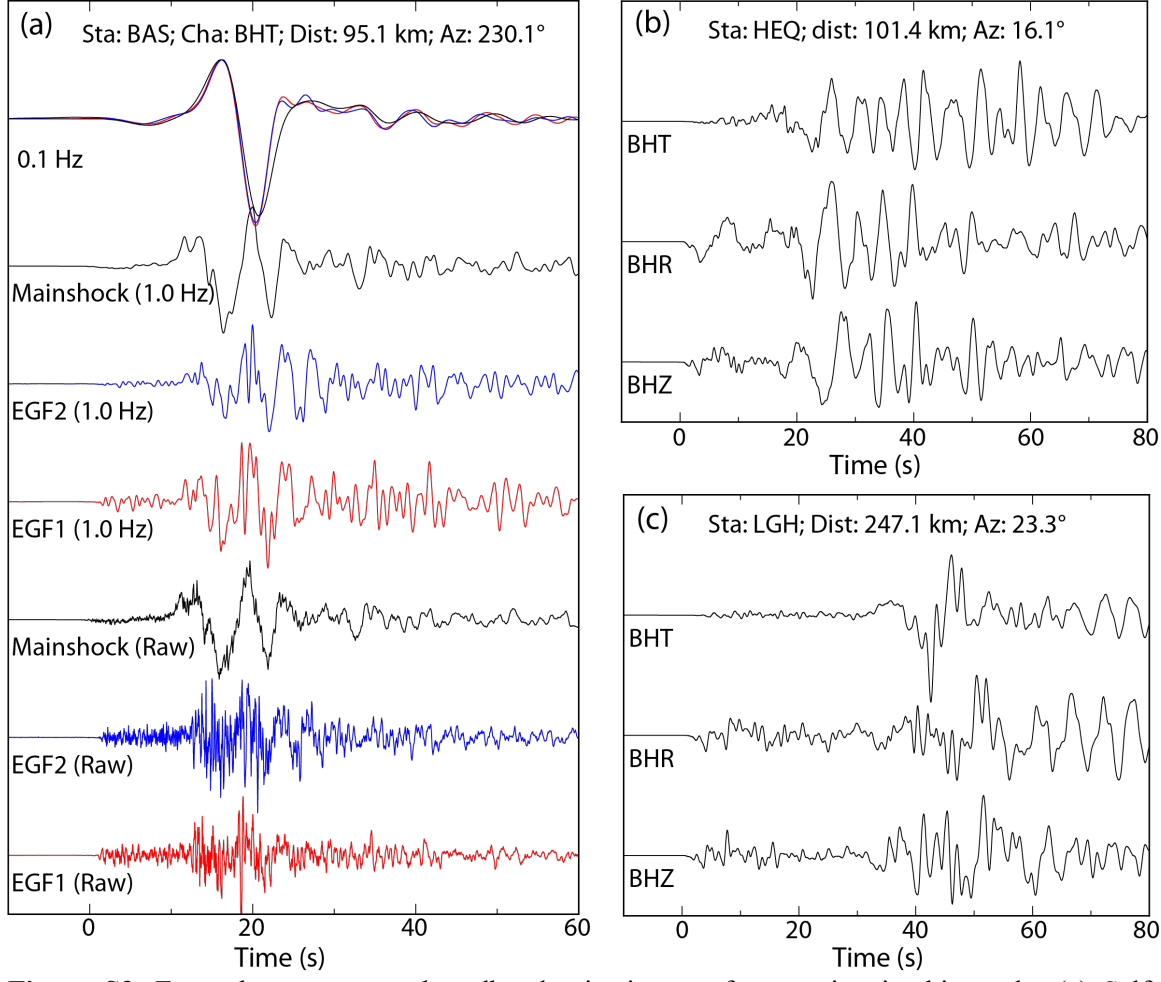


Figure S3. Example near-source broadband seismic waveforms using in this study. (a) Self-normalized transverse recordings at station BAS for the mainshock, EGF1, and EGF2 with different lowpass filters with 1.0 Hz and 0.1 Hz. There is no filter for the raw data. The almost identical waveforms at long period (< 0.1 Hz) suggest similar focal mechanism. (b) and (c) Three-component recordings low filtered with 1.0 Hz for the mainshock at HEQ and LGH, respectively.

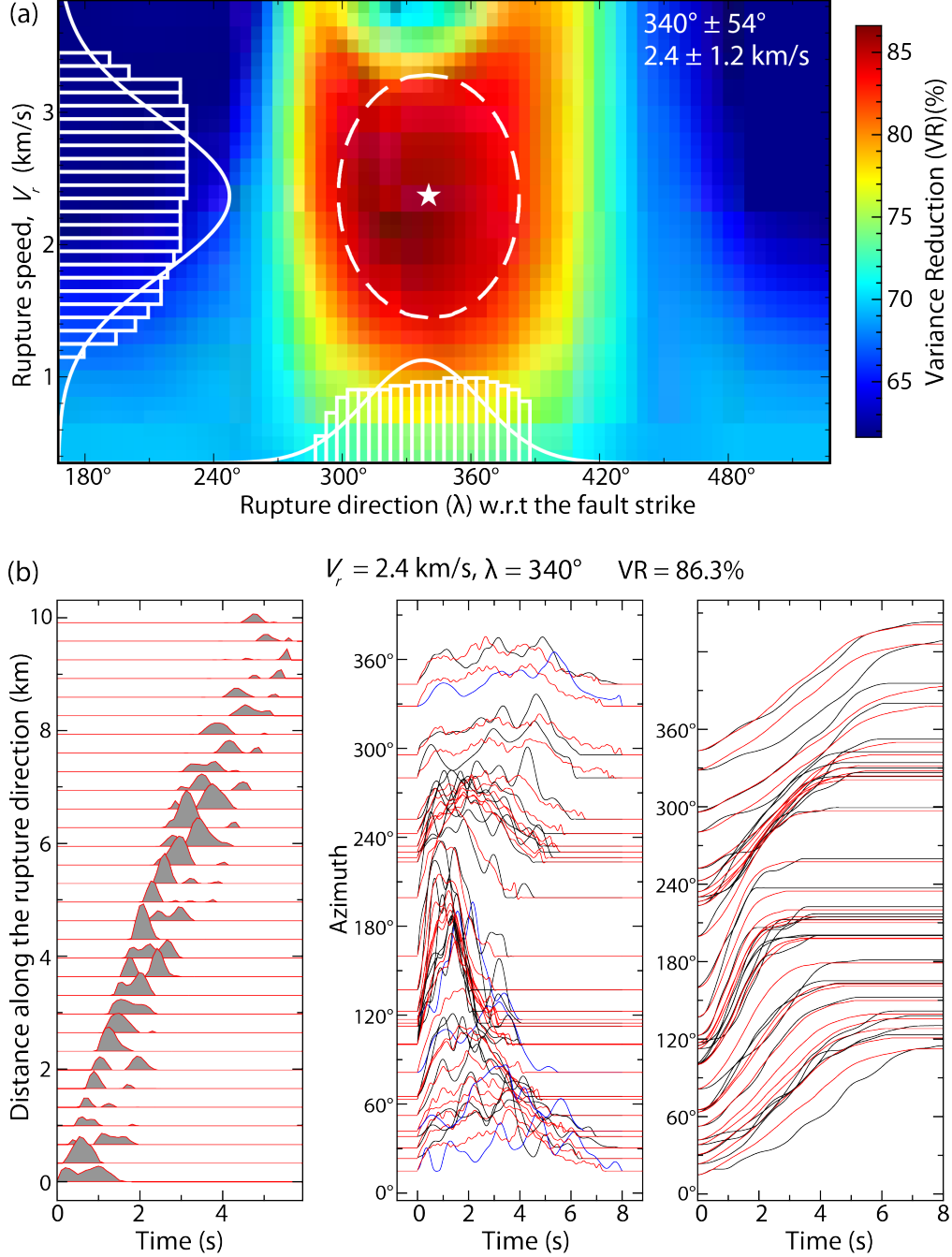


Figure S4. The optimal rupture speed and rupture direction with respect to the fault strike (anti-clockwise) for a line source on the fault plane based on grid search using AMRFs with EGF2 as the EGF earthquake. (a) Variance reductions (VRs) for different rupture speeds and rupture directions on the fault plane (strike = 137° and dip = 75°). VRs larger than $\sim 81\%$ (95% of the maximum of VR) are used to estimate the mean and standard deviation of rupture speed and rupture direction. The dashed ellipse shows 95% confidence. Two histograms show the number of data with $VR > \sim 81\%$. The optimal (white star) and two standard deviations of rupture speed and rupture direction are indicated by the inset numbers. (b) Results for a line source with the optimal rupture speed and rupture direction. The left panel shows the inverted MRLFs. The middle panel shows the deconvolved (black) and synthetic (red) AMRFs. Variance reductions of five AMRFs (blue) at LIG, YYU, DOC, HCB, and DLG with increased azimuths are lower than 80%, and the weights of these AMRFs are 0.3 (rather than 1.0) in the inversion. The right panel shows the corresponding moment time histories.

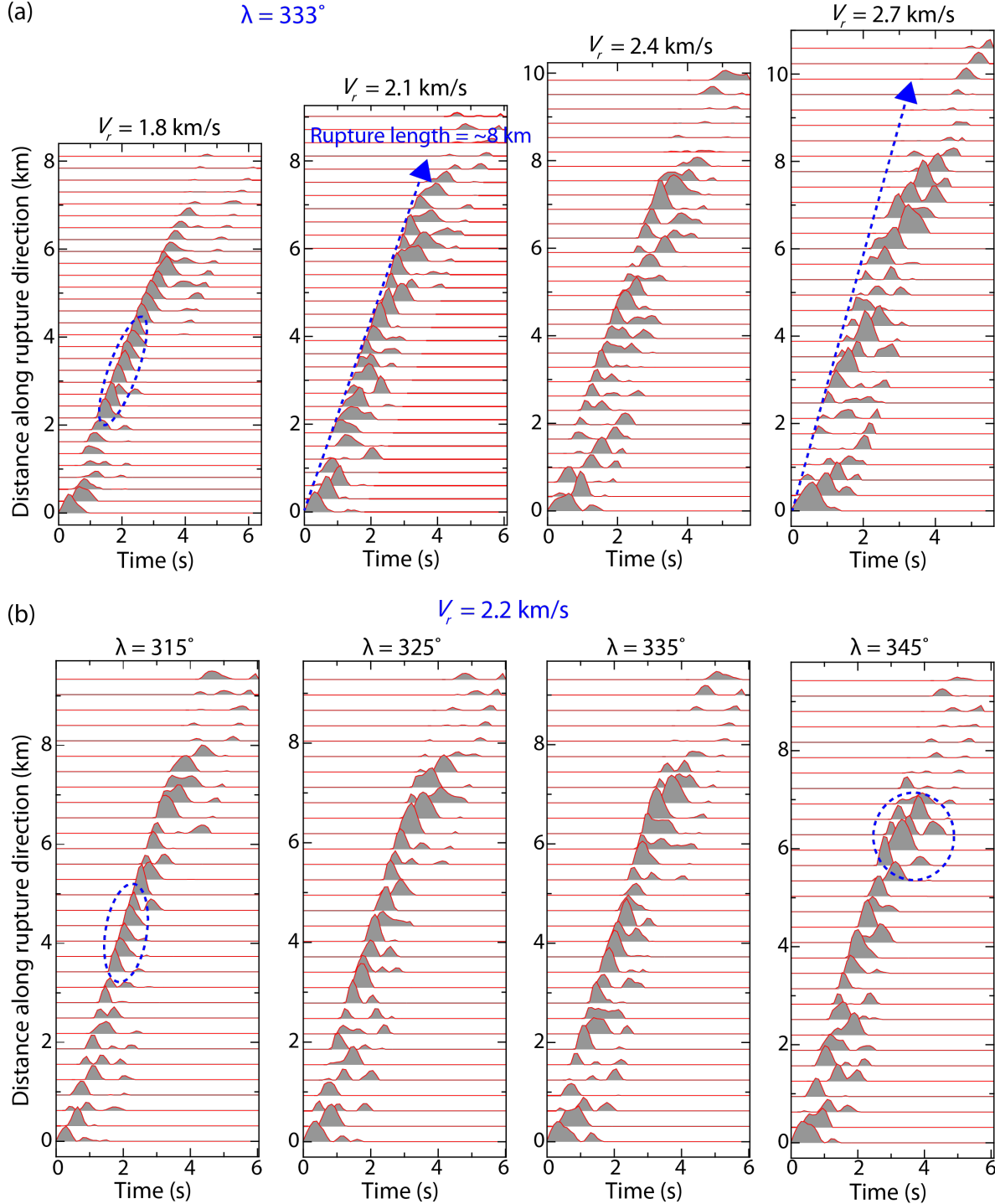


Figure S5. The inverted MRLFs with different rupture speeds and rupture directions. (a) The inverted MRLFs with a rupture direction of 333° and rupture speeds of 1.8 to 2.7 km/s. The MRLFs surrounded by a dashed ellipse are piled up. In the second panel, the dashed arrow indicates a rupture length of $\sim 8.0 \text{ km}$. In the right panel, the beginnings of MRLFs are not aligned well. (b) The inverted MRLFs with rupture directions of 315° to 345° and a rupture speed of 2.2 km/s. In the left panel, The MRLFs surrounded by a dashed ellipse are piled up. In the right panel, the MRLFs surrounded by a dashed ellipse are spread in time.

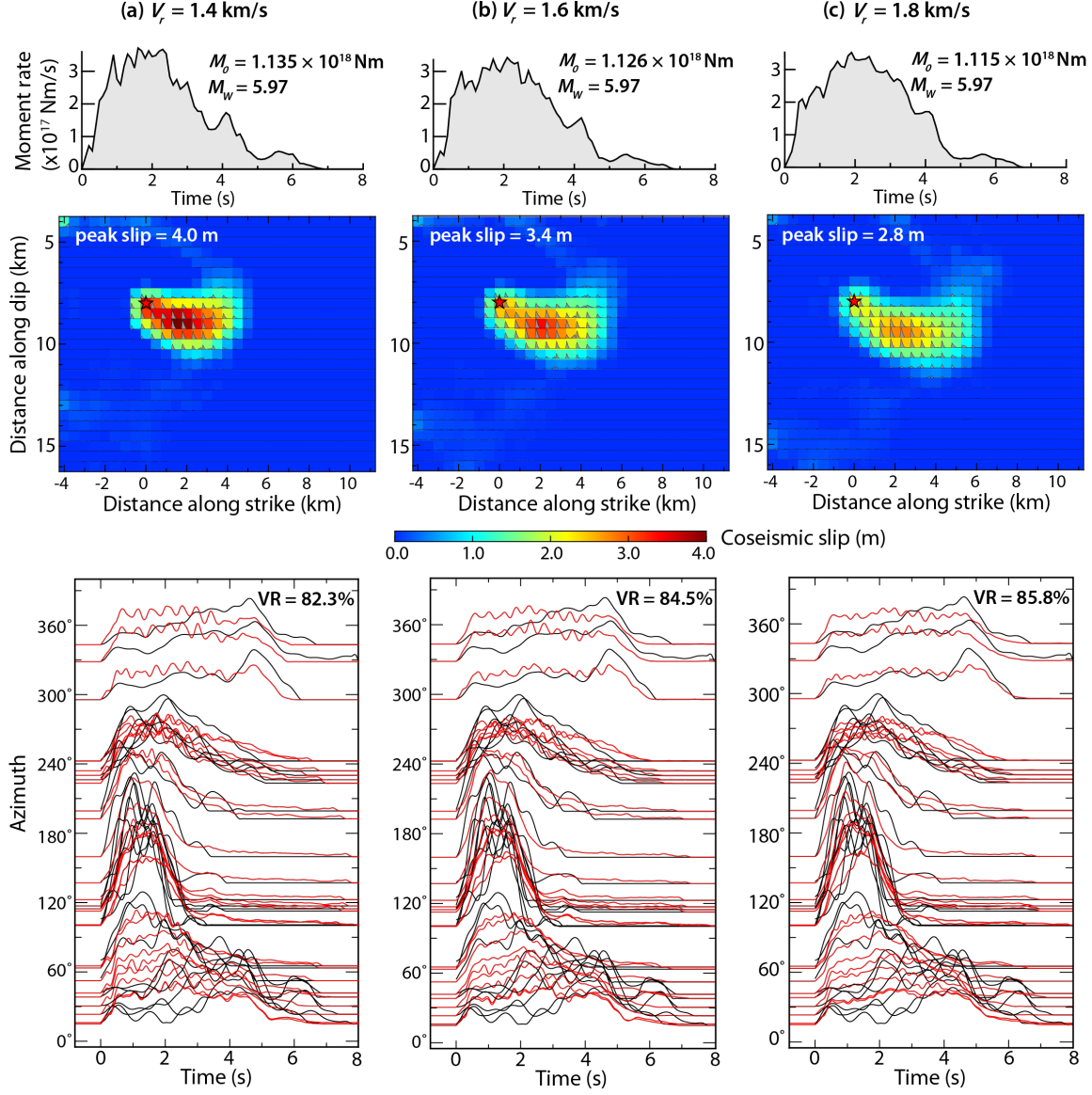


Figure S6. Finite-fault inversions with different assumed rupture expansion speeds of (a) $V_r = 1.4$ km/s, (b) $V_r = 1.6$ km/s, (c) $V_r = 1.8$ km/s, (d) $V_r = 2.0$ km/s, (e) $V_r = 2.2$ km/s, (f) $V_r = 2.4$ km/s, (g) $V_r = 2.6$ km/s, (h) $V_r = 2.8$ km/s, and (i) $V_r = 3.0$ km/s, respectively. The subfault source time functions are shown as gray polygons for those grids with slip larger than 15% of the peak slip. The observation are AMRFs with EGF1. Top panels: moment-rate functions (MRFs); middle panels: coseismic slip distributions; and bottom panels: comparison of synthetic (red) and deconvolved (black) AMRFs.

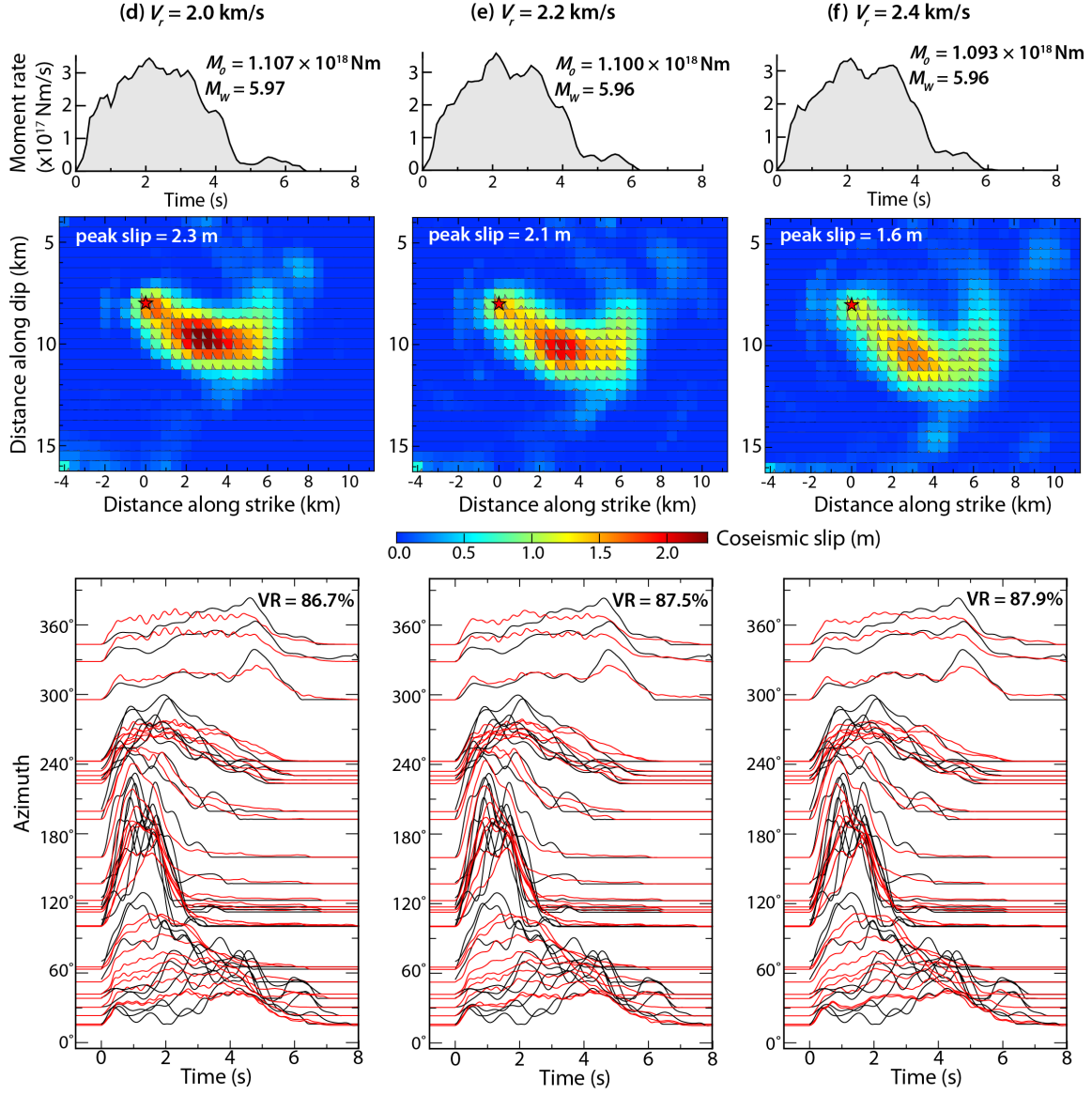


Figure S6. Continued.

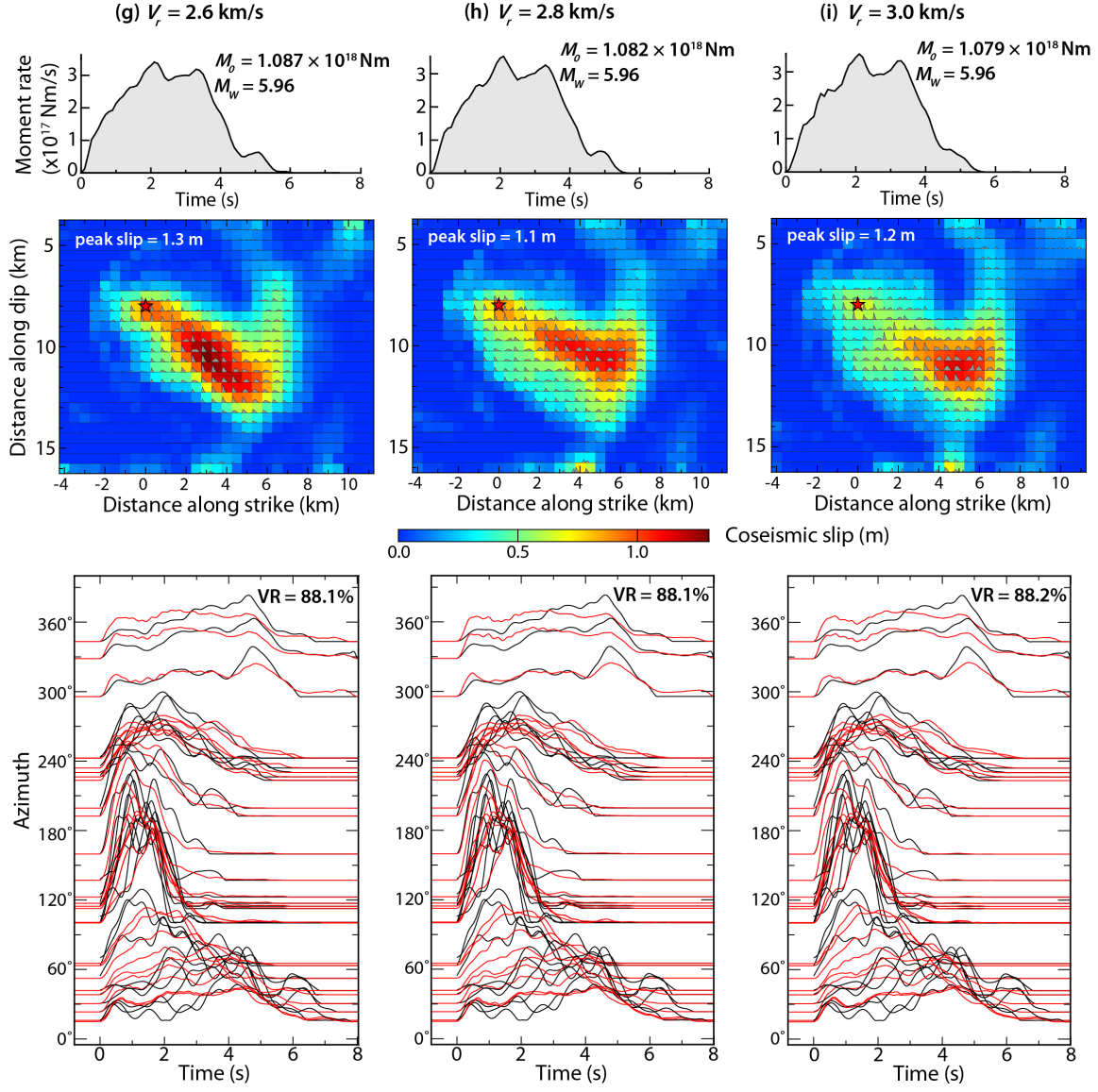


Figure S6. Continued.

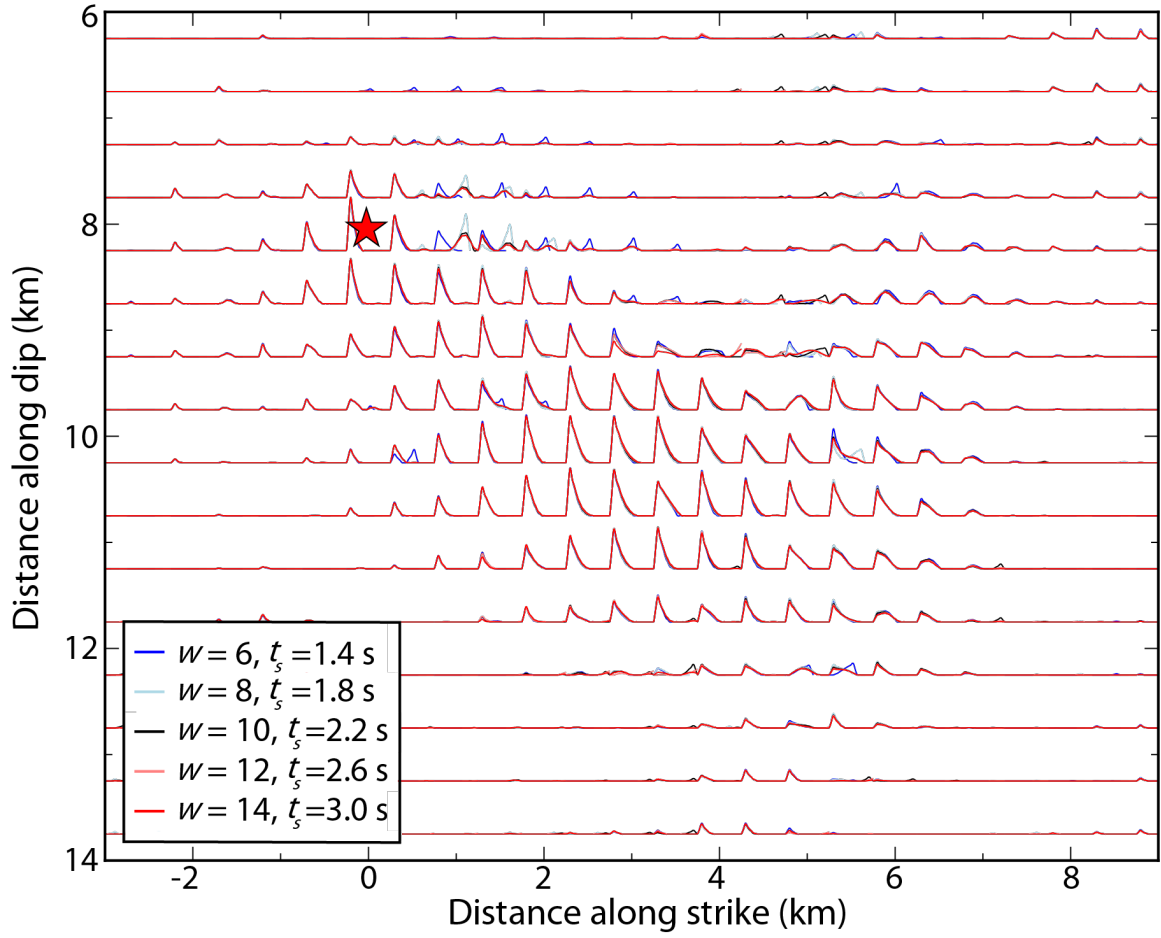


Figure S7. The inverted results of moment rate functions of subfaults with different triangle windows settings. The inversion used the AMRFs data from EGF1 with the rupture seepd V_r of 2.2 km/s. W is the number of windows, and t_s is the allowed max length of moment rate functions. 10 triangles with maximum subfault duration of 2.2 s are used in our preferred slip model (Figure 8b).

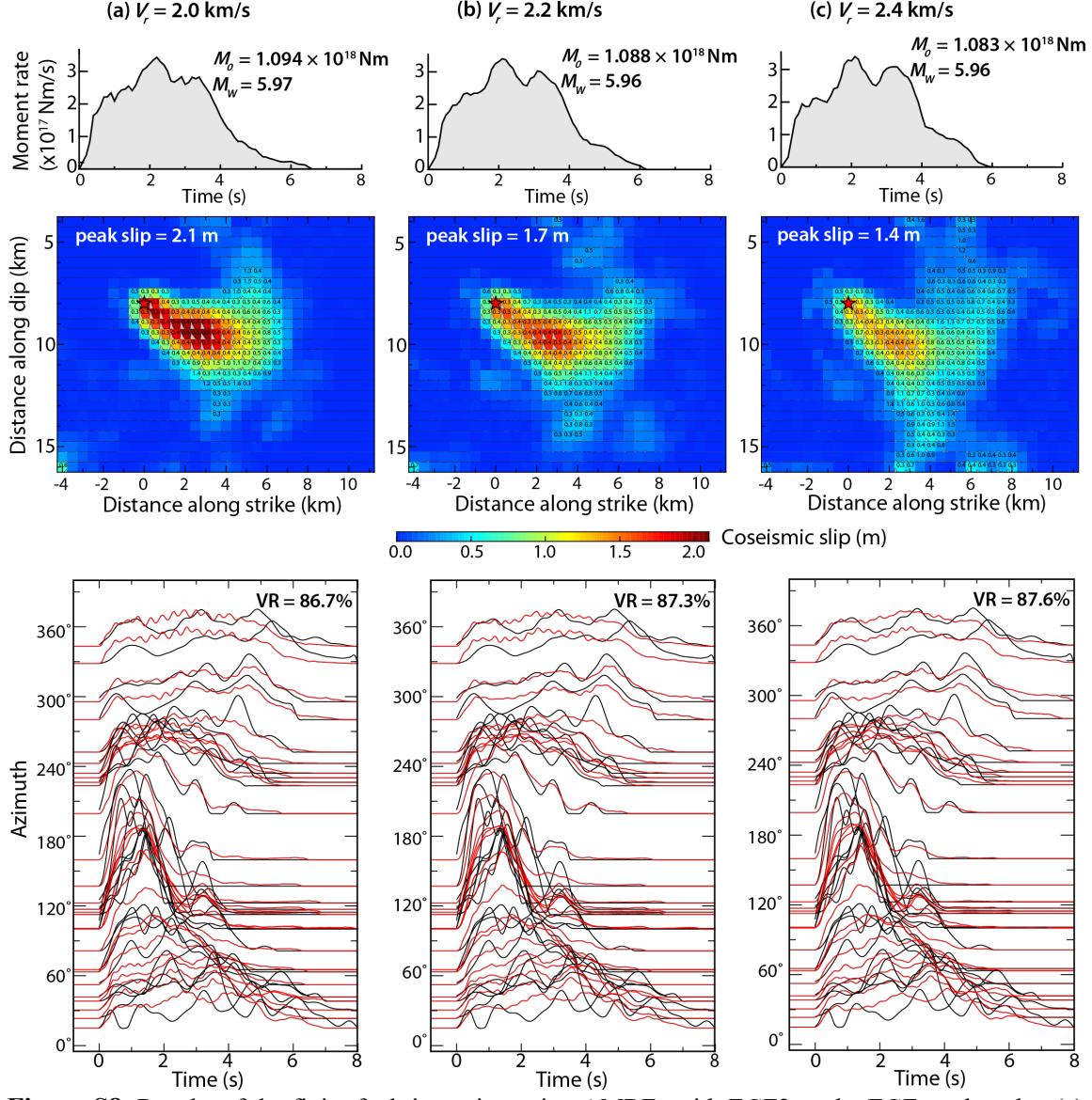


Figure S8. Results of the finite-fault inversion using AMRFs with EGF2 as the EGF earthquake. (a), (b), (c) are the results with $V_r = 2.0 \text{ km/s}$, 2.2 km/s , and 2.4 km/s , respectively. Top panels: moment-rate functions (MRFs); middle panels: coseismic slip distributions subfault source time functions shown by gray polygons and centroid slip duration marked for those grids with slip larger than 15% of the peak slip;; and bottom panels: comparison of synthetic (red) and deconvolved (black) AMRFs.

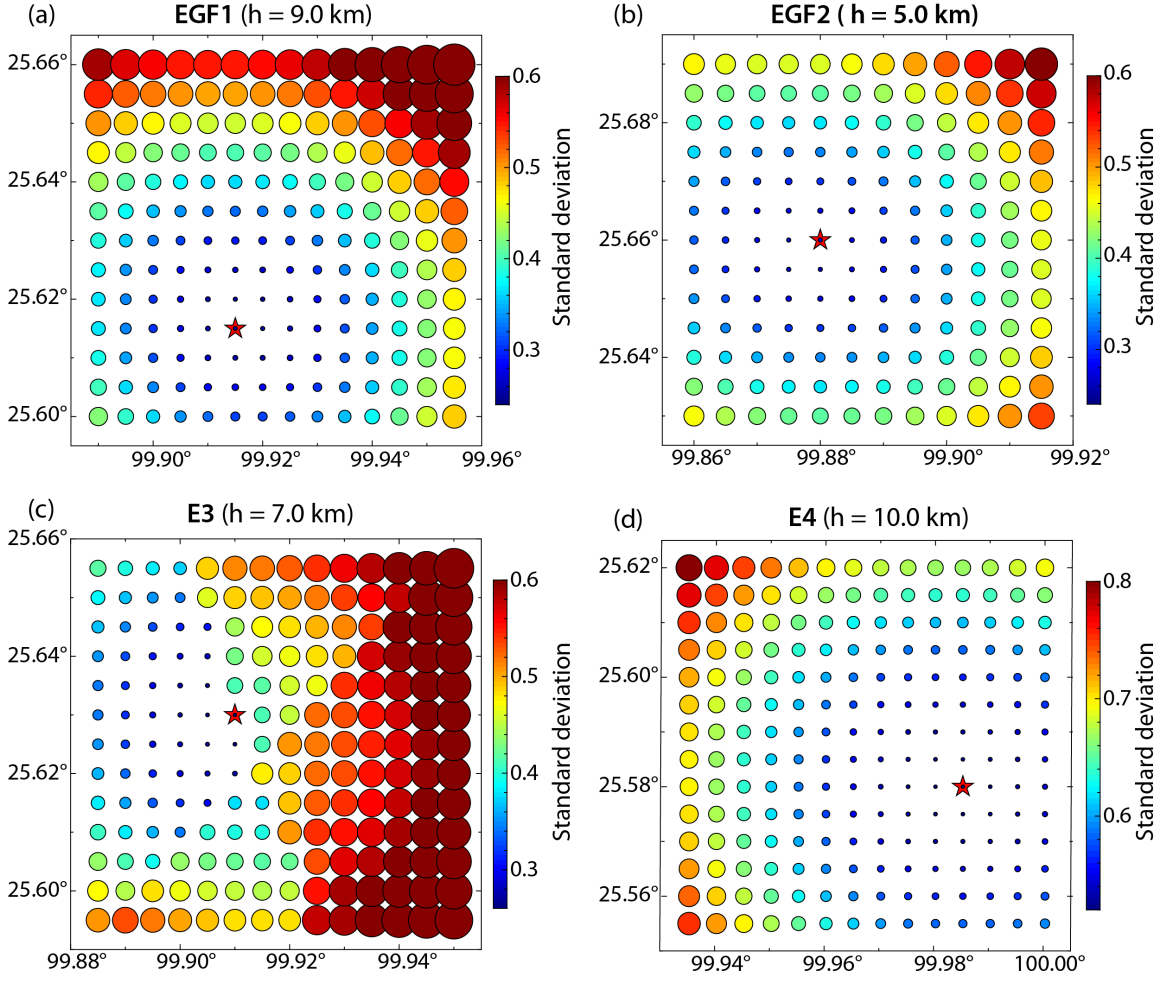


Figure S9. Misfit of P arrival times for (a) and (b) the two EGF events, (c) the largest foreshock (E3), and (d) the largest aftershock (E4). Dots indicate the standard deviation of the synthetic P wave travel time difference between target earthquake and mainshock. Red stars indicate the solution with the minimum error. The optimal source depth from the grid search is labeled for each target earthquake.

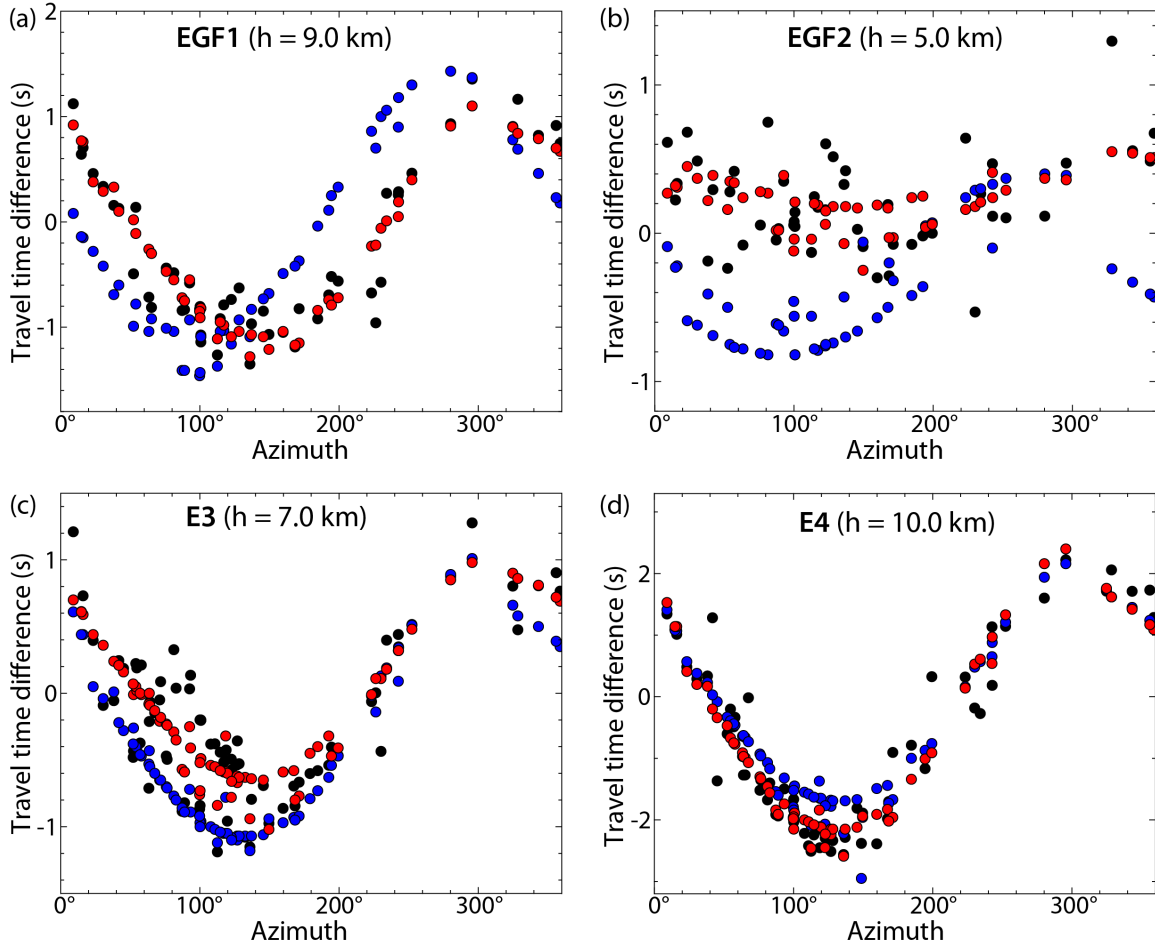


Figure S10. Fitting of the P wave travel time difference of between target earthquakes (EGF1, EGF2, E3 and E4) and mainshock. Black dots show the observed P wave travel time differences. Blue dots show the predicted travel time differences with the locations from the YEA catalog, and red dots are predictions from our relocated results (Figure S9). The optimal source depth from the grid search is labeled for each target earthquake.

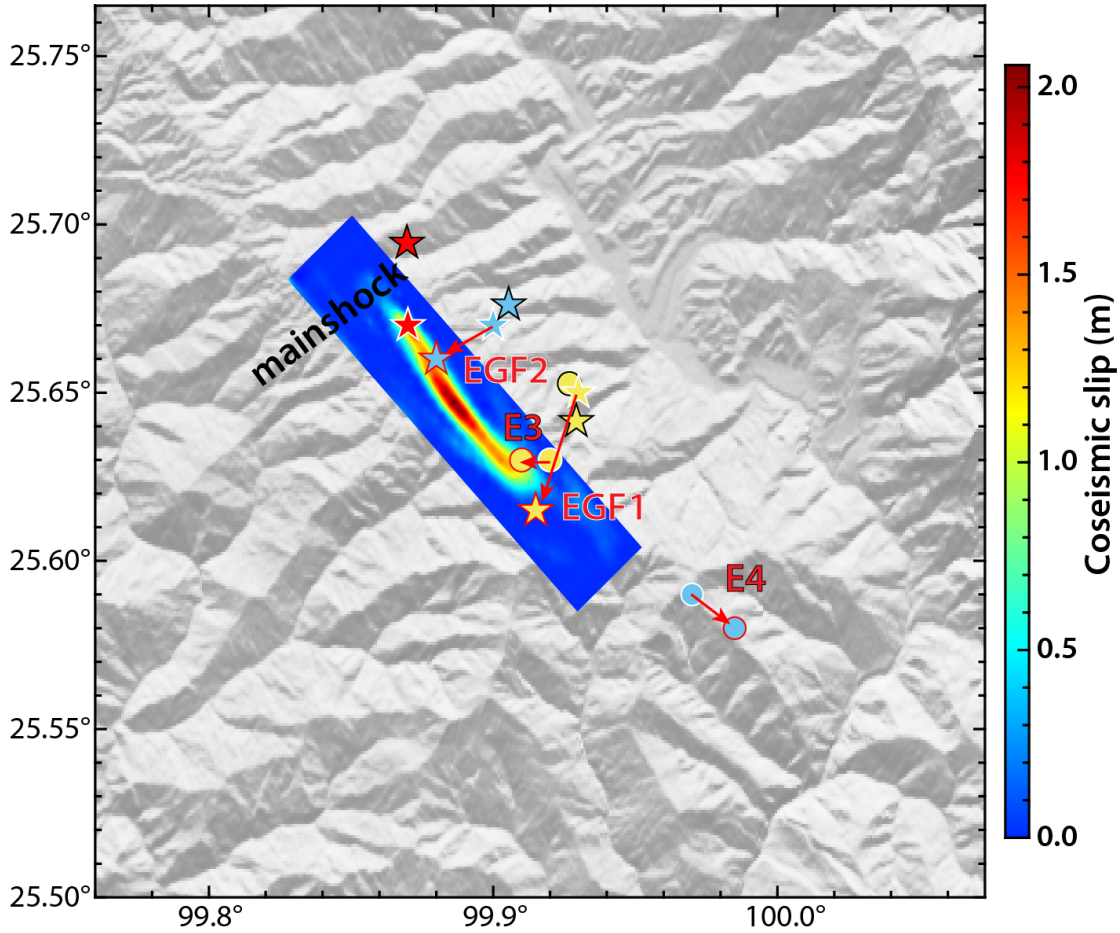


Figure S11. Comparison of our relocation results with the locations from the YEA catalog and the high-precise catalog from Zhou et al. (2021) for the two EGF earthquakes (blue and yellow stars), the largest foreshock (E3; yellow circles) and the largest aftershock (E4; blue circles). Symbols outlined by white indicate locations from the YEA catalog, outlined by black are from the Zhou et al. (2021), and outlined by red are our relocation results. The red star outlined by white and black indicate the mainshock location from the YEA catalog and Zhou et al. (2021), respectively. Arrows indicate the relative location which gives the travel time difference shown in Figure S10.

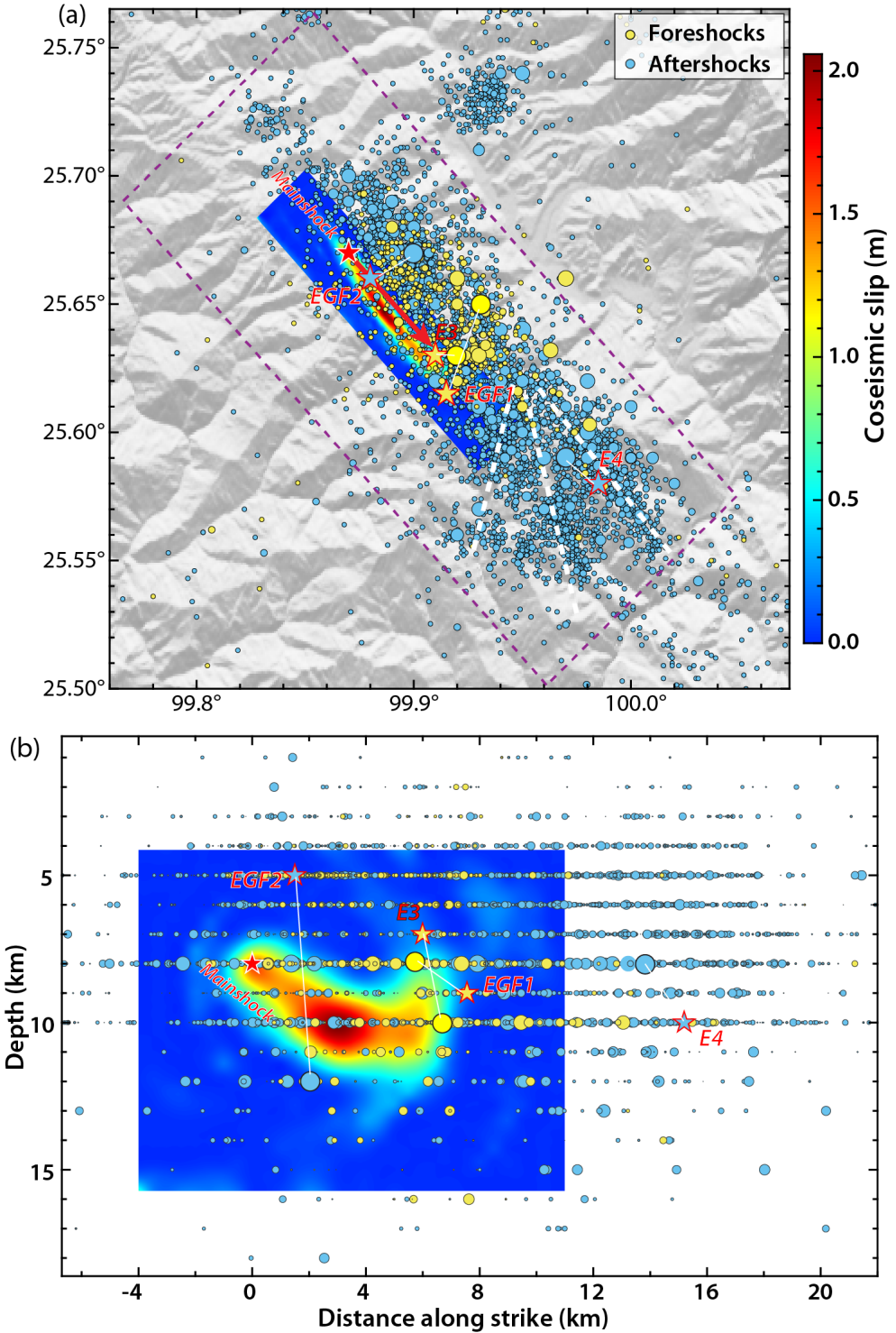


Figure S12. Spatial distribution of our preferred coseismic slip model for the mainshock with the seismicity of foreshock and aftershock activity from the YEA catalog. (a) Our preferred coseismic slip distribution of the Yangbi mainshock (Figure 8b) with the seismicity from the YEA catalog. (b) Depth view of the coseismic slip distribution and seismicity in magenta dashed box in (a) along the fault strike. Stars show the mainshock from the YEA catalog, and our relocated EGF1, EGF2, E3, and E4, with bars connecting the corresponding locations in the YEA catalog. Other symbols are the same as in Figure 11.